Heliyon 9 (2023) e21696

Contents lists available at ScienceDirect

Heliyon

journal homepage: www.cell.com/heliyon

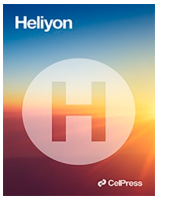

Measurement on the neutron and gamma radiation shielding performance of boron-doped titanium alloy $Ti_{50}Cu_{30}Zr_{15}B_5$ via arc melting technique

Celal Kursun [a,*], Meng Gao [b], Seda Guclu [a], Yasin Gaylan [c], Khursheed Ahmad Parrey [a], Ali Orkun Yalcin [a]

[a] Department of Physics, Faculty of Science, Kahramanmaras Sutcu Imam University, Kahramanmaras, 46100, Turkey
[b] CAS Key Laboratory of Magnetic Materials and Devices, And Zhejiang Province Key Laboratory of Magnetic Materials and Application Technology, Ningbo Institute of Materials Technology and Engineering, Chinese Academy of Sciences, Ningbo, 315201, China
[c] Zonguldak Bulent Ecevit University, Ahmet Erdogan Vocational School of Health Services, Zonguldak, Turkey

ARTICLE INFO

Keywords:
Ti-based alloy
Radiation shielding
Boron-doping
Monte Carlo simulation
Linear attenuation coefficient

ABSTRACT

The significance of radiation shielding is on the rise due to the expanding areas exposed to radiation emissions. Consequently, there is a critical need to develop metal alloys and composites that exhibit excellent capabilities in absorbing neutron and gamma rays for effective radiation shielding. Low-density Ti-based alloys with controlled structural properties can be used for radiation protection purposes. The present research investigates boron-doped Ti-based alloy, $Ti_{50}Cu_{30}Zr_{15}B_5$, which is synthesized by arc melting technique, and its structural, mechanical properties, neutron, and gamma-ray transmission rate were investigated. Monte Carlo N-Particle simulation (MCNP6.2) code is used for calculating the Thermal (2.53×10^{-8} MeV) and fast (2 MeV) neutron transmission ratio (I/I_0) dependent on the sample thickness. The Phy-x program is employed for calculating the gamma-ray LAC, MAC, HVL, TVL, and MFP values. The calculated neutron shielding performance parameters of $Ti_{50}Cu_{30}Zr_{15}B_5$ alloy were compared with materials in the literature. It was found that $Ti_{50}Cu_{30}Zr_{15}B_5$ alloy demonstrated impressive physical characteristics, suggesting that it can serve as a promising alloy for neutron and gamma-ray shielding applications.

1. Introduction

Neutron and gamma radiation are widely used and emitted across many fields today. The applications include composition determination in materials, medicinal treatments, nuclear energy production facilities, as well as scientific research and exploration in space. Researchers have studied and developed various protective measures against ionizing radiation, such as concrete, metal alloys, polymers, and glass, to ensure the safety of individuals exposed to radiation in their workplaces, be it in research or industrial settings [1–10]. Neutrons are shielded with substances having large thermal neutron cross-section, and gamma rays are shielded by high atomic numbers and stable elements such as lead and tungsten. As a result, appropriate radiation protection measures need to be developed depending on the type and energy of radiation [11].

* Corresponding author. Department of Pyhsics, Faculty of Science, Kahramanmaras Sutcu Imam University, Kahramanmaras, 46000, Turkey.
E-mail addresses: celalkursun@ksu.edu.tr, celalkursun@hotmail.com (C. Kursun).

https://doi.org/10.1016/j.heliyon.2023.e21696
Received 14 June 2023; Received in revised form 9 October 2023; Accepted 26 October 2023
Available online 26 October 2023

There has been extensive use of substances having high thermal neutron-cross-sections including B, Cd, Sm, and Gd in the field of thermal neutron shielding. Woosley et al. showed that after adding 20 % boron nitride to the thermoplastic polymer, the thermal neutron flux was reduced by 20 % [12]. Toyen et al. showed that the thermal neutron flux was reduced from 95 % to 30 % when different proportions of B_2O_3 were added to paraffin, ranging from 0 % by weight to 35 % by weight [13]. In a different study, Soltani et al. raised the amounts of boron in high-density polyethylene (HDPE) by 1 %, 2 %, and 5 % and discovered that the macroscopic thermal neutron cross-section improved from 0.29 cm^{-1} to 1.23 cm^{-1} [14].

Materials having characteristics like high density, high melting point, high mechanical strength, superior corrosion resistance, and low cost are crucial in the field of radiation shielding. Generally, high-density substances like concrete and lead have been employed to shield gamma radiation [15]. For instance, the lead (Pb) which possesses inherent disadvantages, such as significant toxicity, limited mechanical strength, and relatively low melting point is thus unsuitable for use in radiation shielding [16]. Therefore, titanium-based alloy is considered a good alternative in radiation shielding applications because it is a tougher material compared to lead, which has been studied in the previous literature [15,17–19]. For instance, Senkov et al. [20] previously investigated the compression, microstructure, and deformation properties across various temperatures for four distinct Ti-based high entropy alloys (HEAs). $Al_{10}Cr_{20}Mo_{20}Nb_{20}Ti_{20}Zr_{10}$ (Waseem et al. [21]), $Al_{35}Cr_{14}Mg_6Ti_{35}V_{10}$ (Chauhan et al. [22]), and MgAlMnFeCu (Pandey et al. [23]) are a few other alloys documented in literature that have been synthesized and the results obtained from different measurement techniques were analysed. Until the recent past there has not been a sufficient research published specifically on Ti–Cu–Zr–B metal alloys for radiation shielding applications. The current research, however, leads to the production of such alloy composites and deduce their potential for application in nuclear radiation protection.

In the present study, the alloy with a composition of $Ti_{50}Cu_{30}Zr_{15}B_5$ was synthesized from pure elemental metals by employing an arc melting technique in a titanium-gettered inert environment. The element boron can have significant impacts on alloy microstructure and properties due to its influence on grain size, phase transformation, and mechanical properties. In our study, the boron element was added to the alloy to promote the formation of fine-grained microstructures, leading to improved physical properties like mechanical strength and hardness. The synthesized $Ti_{50}Cu_{30}Zr_{15}B_5$ alloy, featuring distinct phases including TiB, Ti_2Cu, and $Cu_{10}Zr_7$ underwent characterization by XRD, SEM, and DTA (differential thermal analysis) techniques. The Vicker's microhardness test is used to evaluate the sample's hardness. The primary aim of this research is to measure the performance of the resultant alloy in terms of shielding against neutron and gamma-ray radiation.

2. Methods

2.1. Experiment

$Ti_{50}Cu_{30}Zr_{15}B_5$ alloy was synthesized using boron (B) in the form of ingots via arc melting technique from the main composition of the Ti–Zr–Cu system. The alloy was produced under an environment-controlled system using the pure elements Ti (99.99 %), Cu (99.7 %), Zr (99.9 %), and B (99.5 %), in a titanium-gettered argon atmosphere. The obtained ingot was remelted multiple times to achieve a chemically homogeneous $Ti_{50}Cu_{30}Zr_{15}B_5$ alloy, which was characterized by several techniques before evaluating its neutron and gamma-ray radiation shielding performance. The cast ingots were sliced with a precision diamond saw to prepare the samples for the following characterizations. During the sample preparation, the polycrystalline diamond suspension was applied for fast stock removal and for creating a perfectly smooth texture ready for measurements.

Powder X-ray diffraction was undertaken using a Philips X'Pert – MPD diffractometer with Cu K_α radiation ($\lambda = 0.15406$ nm) generated at 40 kV and 30 mA. The diffraction pattern was recorded over a wide range of angles (2θ) from 20° to 100° with a scanning rate of 2°/min. The Philips XL-30 FESEM equipped with a modern EDS system was used to study the sample morphology and chemical composition. Using a PerkinElmer's Diamond TG/DTA thermal analyzer, the alloy's thermal behavior was examined from differential thermal analysis (DTA) at a constant heating rate of 20 °C/min between 50 °C and 1200 °C in a flowing argon environment. Using a Shimadzu HMV-2 microhardness tester with a force of 0.98 N for 10 s, the Vickers microhardness test was conducted. Before determining the surface hardness of the alloy with a microhardness measuring device, the material surface was examined under an optical microscope. In the results and discussion section, we made an effort to explain the details of our analysis. The density measurement for the $Ti_{50}Cu_{30}Zr_{15}B_5$ alloy, required for neutron and gamma-ray shielding calculations, is obtained using the Archimedes principle with a WSA224 density measurement kit in deionized water. Monte Carlo N-Particle simulation package is used for calculating the thermal and fast neutron transmission ratio (I/I_0) dependent on the sample thickness. The variation of radiation shielding performance parameters, LAC, MAC, HVL, TVL, and MFP for gamma radiation are studied with photon energy using Phy-x program.

2.2. Monte Carlo simulation

In situations where experimental conditions pose constraints or prove difficult to achieve, statistical models such as the Monte Carlo method offer effective numerical solutions for addressing physical challenges. One notable simulation tool, known as MCNP code (Monte Carlo N-particle radiation transport code), is adept at handling complex three-dimensional geometries and finds extensive applications in diverse fields including radiation shielding, reactor design, dose computations, and medical imaging [24].

It was reported that the MCNP code has been utilized to estimate the radiation shielding capabilities of a variety of materials, including concrete [25], glasses [26], and metal alloys [9]. In the present research, we computed the thermal and fast neutron transmission rate based on the shield thickness using the MCNP6.2 version of the program.

As depicted in Fig. 1, the simulation setup comprises a focused mono-energetic neutron source positioned within a cylindrical

chamber, alongside the target material, and a specialized detector (F4 Tally) designed to quantify the neutron flux passing through the sample.

In this study, we prepared the target material by uniformly mixing the $Ti_{50}Cu_{30}Zr_{15}B_5$ alloy, which has a density of 5.8 g/cm^3. The thermal neutrons were defined at 2.53×10^{-8} MeV while the fast energy neutrons were set as having 2 MeV. The distance between the neutron source and the target material, as well as the distance between the target material and the detector, were both set to 50 cm. To calculate the detector flux, we used the F4 tally feature of MCNP6.2, which measures the average flux per square centimeter per source particle. For each simulation, we generated 10^7 neutron histories, and the statistical error remained below 1 % in all simulations. The source and target distance were chosen to ensure a relatively uniform neutron flux distribution over the target area. Source and target distance is so chosen that it allows for some neutron scattering and absorption effects, which could be relevant to certain experiments and simulations. The detector should not count the neutrons that are emitted from the source but don't interact with the sample. The geometry was designed so that it could not consider the neutrons that scatter and reach the detector. Simulation geometries like this have been used as one can find in literature.

2.3. Theoretical Basis of gamma ray shielding

The attenuation principle, which asserts that a barrier material blocks or bounces particles and reduces the effectiveness of waves or rays, underlies the behavior of radiation shielding. The linear attenuation coefficient (LAC, μ), mass attenuation coefficient (MAC, μ_m), mean free path (MFP), half value layer (HVL), tenth value layer (TVL), and neutron attenuation of alloys should all be studied as a result.

The widely recognized Beer-Lambert law offers a means to calculate the linear attenuation coefficient (μ), which quantifies the likelihood of an interaction occurred between gamma rays and medium, the linear attenuation coefficient (μ) has been defined through equations (1) and (2) as:

$$I = I_0 e^{-\mu x} \tag{1}$$

$$\mu_m = \left(\frac{\mu}{\rho}\right) = \frac{\ln\left(I_0/I\right)}{\rho x} \tag{2}$$

where I_0 represents the initial un-attenuated photon intensity, and I signify the attenuated photon intensity, μ (cm^{-1}) and μ_m (cm^2/g) denote linear and mass attenuation coefficients, and x (cm) and ρ (in g/cm^3) refer to the material's the thickness and density.

The half-value layer (HVL) and the Tenth value layer (TVL) represent the thicknesses needed to decrease the radiation intensities by 50 % and 90 %, respectively. These values can be derived from the linear attenuation coefficient (μ) as (equations (3) and (4)) follows:

$$HVL = \frac{0.693}{\mu} \tag{3}$$

$$TVL = \frac{2.302}{\mu} \tag{4}$$

The Mean Free Path (MFP) parameter quantifies the average distance between two photon interactions and can be determined from μ (in cm^{-1}) through equation (5).

$$MFP = \frac{1}{\mu} \tag{5}$$

3. Results and discussion

The structural, thermal, and mechanical properties of the $Ti_{50}Cu_{30}Zr_{15}B_5$ alloy were investigated using XRD, SEM, DTA, and Vickers microhardness measurements. XRD and SEM measurements confirmed that the produced alloy was chemically homogeneous. Three distinct phases were identified in the case of $Ti_{50}Cu_{30}Zr_{15}B_5$ alloy as demonstrated in the x-ray diffraction pattern and SEM micrographs as shown in Figs. 2 and 3 (a). The diffraction peaks obtained in $Ti_{50}Cu_{30}Zr_{15}B_5$ alloy correspond to the hexagonal TiB (black), titanium-rich crystals of the tetragonal Ti_2Cu (dark grey), and crystallites of the orthorhombic $Cu_{10}Zr_7$ (light grey) phases. The

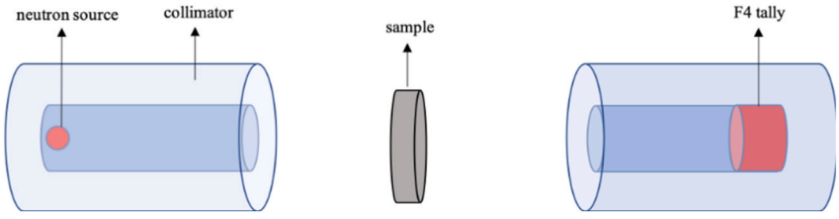

Fig. 1. The geometry of the simulation setup.

strong diffraction peak obtained at 2 $\theta = 39.25°$ was ascribed to the Ti_2Cu phase since it contained the highest titanium amount compared to other phases. All the reflections exhibited in an X-ray diffractogram were indexed in accordance with the earlier studies reported [27–33]. Therefore, the formed phases in $Ti_{50}Cu_{30}Zr_{15}B_5$ alloy were orthorhombic $Cu_{10}Zr_7$, hexagonal TiB, and tetragonal Ti_2Cu, respectively.

The melting temperatures of the constituent components that make up the alloy are relatively close to each other. To ensure the homogeneity of the resulting alloy, the process of heating and cooling of constituent components forming the alloy was repeated several times. The homogeneity of the mixture and composition of the alloy was revealed from the analysis of the results obtained from SEM-EDX measurements as shown in Figs. 3(a) and Fig. 4. The micrographs obtained from SEM and optical microscopy reveal the microstructure of the alloy after solid solution heat treatment. The conventionally solidified $Ti_{50}Cu_{30}Zr_{15}B_5$ alloy was characterized by grainy microstructure and the size of grains was found to be less than 10 μm. The weight percentage (content ratio) of the elements in the resulting alloy after production was found to be identical to that incorporated before production. In other words, the EDX measurement reveals that the chemical composition is fairly consistent with the nominal value. Therefore, there was no reduction, evaporation, or weight loss of materials observed during the synthesis process. The stoichiometric ratio of the elements in $Ti_{50}Cu_{30}Zr_{15}B_5$ alloy was confirmed qualitatively and quantitatively by EDX analysis (inset Fig. 4). From the SEM micrograph, it was observed that the three phases with different crystal geometries were uniformly distributed throughout the sample. A grain size distribution plot was drawn using Image J software and provided in Fig. 3 (b). The grain sizes are not uniform; however, the distribution of the grains is homogenous. The sample's mean grain size is determined by fitting the grain size distribution histogram to the log-normal distribution function in the origin. The resulting average grain size is found to be 1.75 μm.

The as-synthesized alloy was briefly characterized before being put through a thermal behavior investigated by the DTA instrument. All the phases observed in the as-cast state were seen to be dissolved after solutionizing the alloy at 910 °C, which was confirmed by SEM micrographs. DTA analysis of the crystalline $Ti_{50}Cu_{30}Zr_{15}B_5$ alloy provided information about the melting temperature (910 °C) associated with the endothermic peak. The small endothermic peak identified at 853 °C (Fig. 5) can be attributed to the allotropic phase transition of commercial-grade titanium since it exhibits a crystal structure transformation from a hexagonal structure (α-phase) to a volume-centered cubic structure (β-phase) [34]. Several studies have been performed in the past on how Zr affects the phase transition of pure Ti. It was found that β to α + β and α to α + β phase transition temperatures of Ti can be reduced by adding Zr in amounts less than 50 at% based on the reported research [35]. Pure titanium undergoes an allotropic transformation at 882.8 °C, while the TiB phase contains 5.1 % boron according to the titanium-boron phase diagram, and is in alpha phase up to 883 °C [36,37]. For this reason, the boron content of the alloy does not affect the phase transition temperature and therefore it can be concluded that the endothermic peak observed in the thermograph was due to the 15.3 % Zr content in the $Ti_{50}Cu_{30}Zr_{15}B_5$ alloy. The solidification peak does not show up on the DTA thermograph because the titanium and boron react completely to create the TiB phase. It was also reported by J. Abenojar et al. that aluminum-boron reactions exhibit similar thermal behavior [38].

Prior to the material's microhardness measurement, the surface was sanded with 600, 800, 1000, and 1200 mesh abrasives and then polished with the aid of diamond suspension solutions to ensure a clear observation of the material surface. Vickers microhardness values of $Ti_{50}Cu_{30}Zr_{15}B_5$ ingot alloy produced with CS are depicted in Fig. 6. The Vickers microhardness (HV) method of the alloy composite is carried out with a load of 0.98 N for 10 s. To evaluate the microhardness value of the processed alloy, 10 Vickers' micro-indentations were made. An optical image of the sample showing the microstructure and trace of the pyramid shape on the sample alloy is also incorporated with the microhardness graphic in Fig. 6. As can be seen from Fig. 6, $Ti_{50}Cu_{30}Zr_{15}B_5$ alloy hardness value is 556 HV (±11). Adding boron element (@ 5 %) in Ti–Cu–Zr ternary alloy plays an active role in improving the hardness of the alloy. Moreover, according to the available literature, there exists a linear relationship between boron concentration and material hardness.

The thermal and fast neutron transmission ratio of the $Ti_{50}Cu_{30}Zr_{15}B_5$ alloy was theoretically computed by employing the MCNP6.2 simulation code. The change of thermal and fast neutron transmission ratio with the sample thickness was indicated graphically in

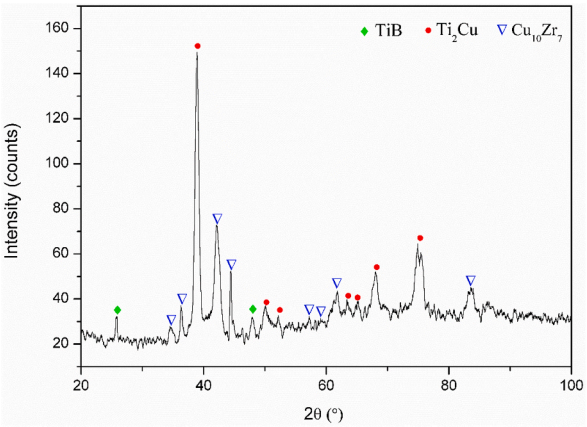

Fig. 2. XRD analysis of $Ti_{50}Cu_{30}Zr_{15}B_5$ alloy.

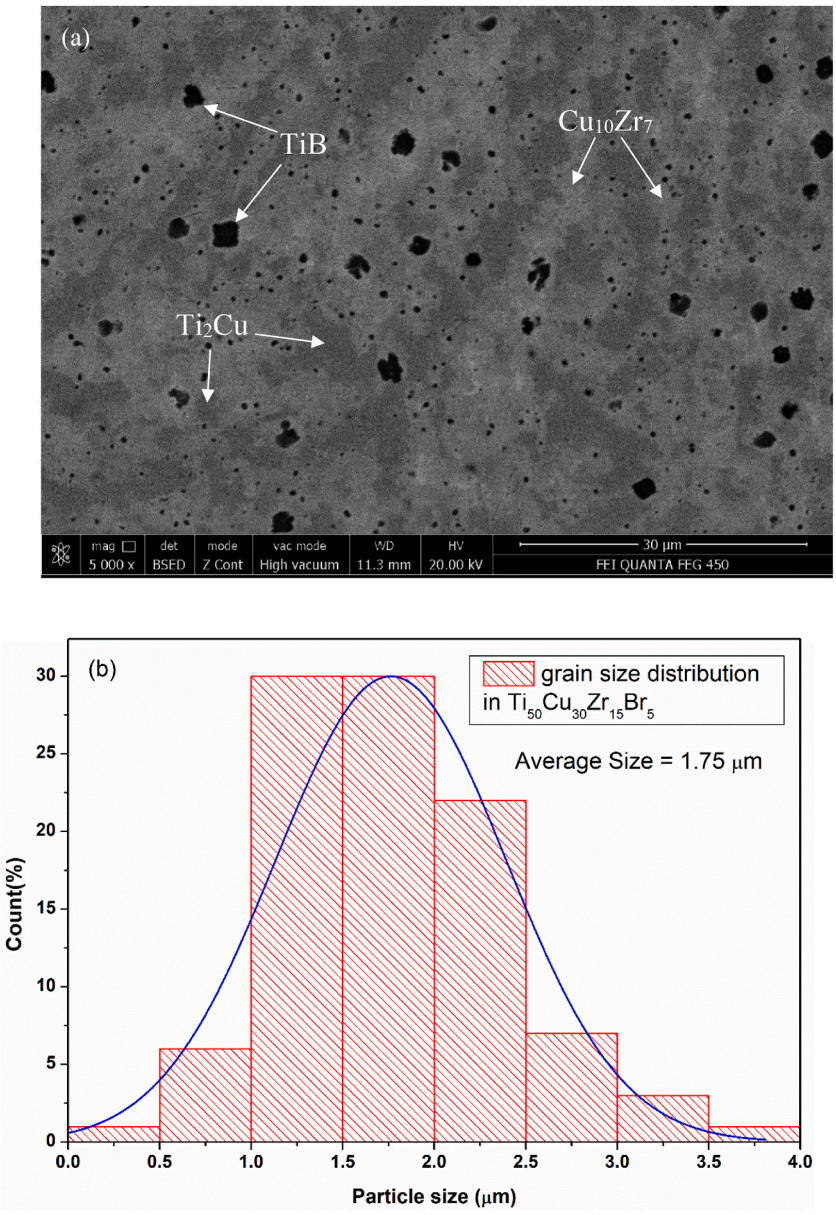

Fig. 3. (a) Indicating SEM image of $Ti_{50}Cu_{30}Zr_{15}B_5$ alloy and (b) Grain size distribution of the sample fitted with a log-normal distribution function.

Figs. 7 and 8, respectively. There was an exponential decay observed in the neutron transmission ratio (I/I_0) with respect to the sample thickness. The ratio was reduced to zero at a sample thickness of over 2 cm, which shows that the neutrons can be almost shielded. Moreover, the fast neutrons also showed the same trend. However, the sample alloy couldn't block them entirely. The transmission ratio of 0.1 cm thick thermal neutrons is 73 %, while it is 0.18 % at 2 cm thickness. $Ti_{50}Cu_{30}Zr_{15}B_5$ alloy showed good thermal neutron shielding performance at 2 cm thickness. The rate of fast neutron transmission at 0.1 cm thickness was 97.7 %, and it was calculated as 63.6 % at 2 cm and 32 % at 5 cm thickness.

The Linear Attenuation Coefficient (LAC) values of the $Ti_{50}Cu_{30}Zr_{15}B_5$ alloy, depending on the photon energy varying from 1.5E-2 MeV–15 MeV, are shown in Fig. 9. While the LAC value was 264.2 cm^{-1} at 1.5E-2 MeV energy photons, it decreased to 0.184 cm^{-1} with 15 MeV energy photons. The Mass Attenuation Coefficient (MAC) $Ti_{50}Cu_{30}Zr_{15}B_5$ alloy is shown in Fig. 10. While the MAC value was 45.5 cm^2/g for 1.5E-2 MeV energy photons and it reduced to 0.032 cm^2/g with 15 MeV energy photons.

When the MAC value of the produced alloy is compared with other materials, it is clear that ordinary concrete, steel-scrap, ilmenite-limonite, and basalt-magnetite have higher values [39]. Additionally, based on the existing literature, we offer a comparative graphic illustrating how the mass attenuation coefficient (μ_m) varies as a function of energy (MeV) for a few common substances (ordinary concrete; OC, steel-scrap; SS, steel-magnetite; SM) and titanium-based alloys ($Ti_{16.33}V_{16.32}Zr_{30.74}Nb_{36.61}$; HEA1,

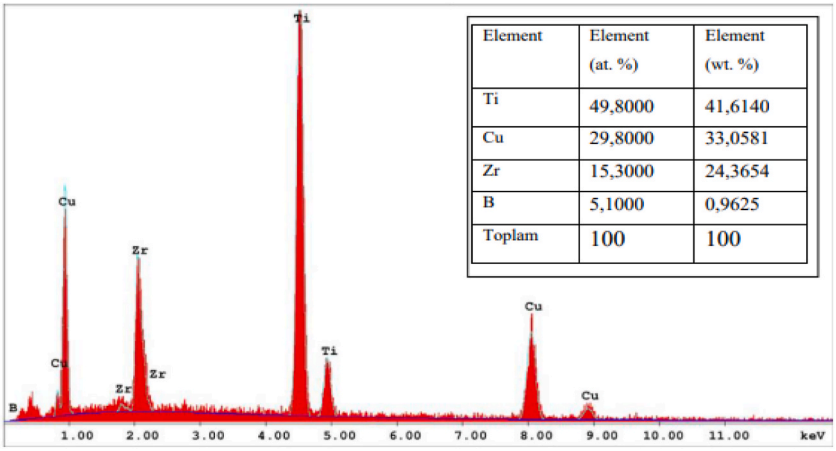

Element	Element (at. %)	Element (wt. %)
Ti	49,8000	41,6140
Cu	29,8000	33,0581
Zr	15,3000	24,3654
B	5,1000	0,9625
Toplam	100	100

Fig. 4. EDX analysis of $Ti_{50}Cu_{30}Zr_{15}B_{5}$ alloy.

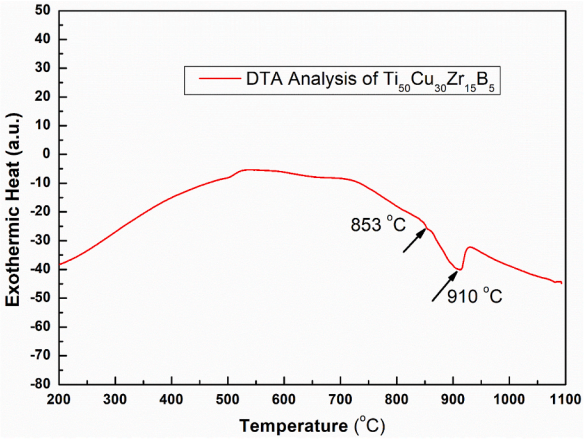

Fig. 5. DTA analysis of $Ti_{50}Cu_{30}Zr_{15}B_{5}$ alloy.

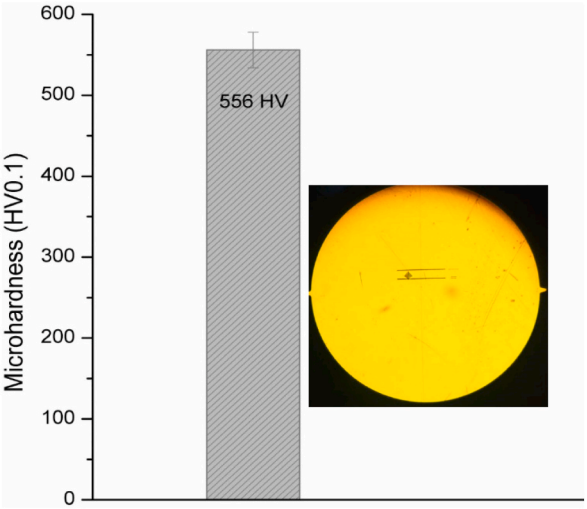

Fig. 6. $Ti_{50}Cu_{30}Zr_{15}B_{5}$ alloy Vickers microhardness analysis.

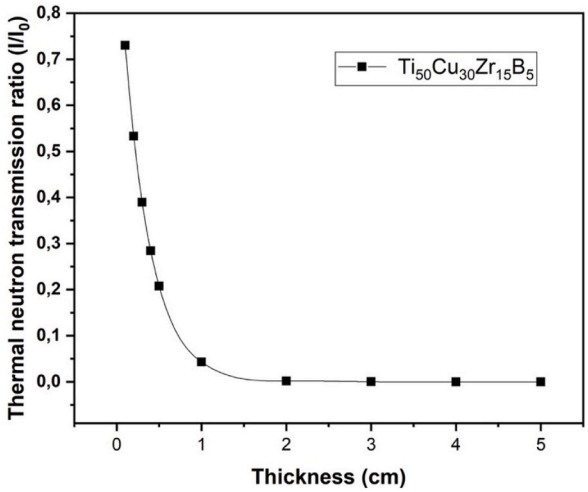

Fig. 7. Thermal neutron transmission rate of $Ti_{50}Cu_{30}Zr_{15}B_5$ alloy.

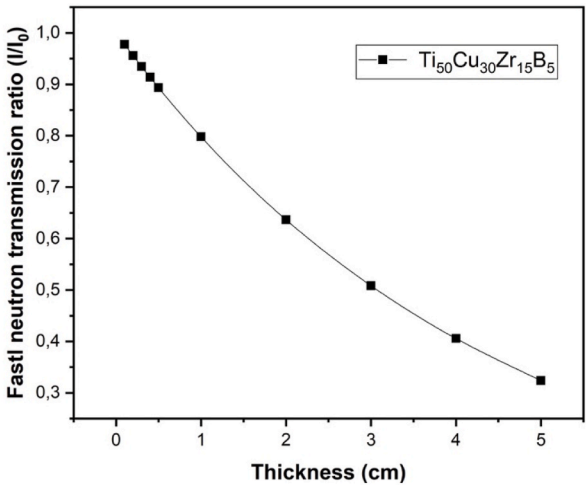

Fig. 8. The fast neutron transmission rate of $Ti_{50}Cu_{30}Zr_{15}B_5$ alloy.

$Ti_{44.09}Sc_{27.61}Al_{16.57}Mg_{7.46}Li_{4.26}$; HEA5, $Ti_{13.76}Al_{3.88}Cr_{14.95}Zr_{13.11}Nb_{26.71}Mo_{27.58}$; HEA8). The graphic for comparison is provided in Fig. 11 below.

The computed MAC values were compared with those of the most extensively utilized shielding materials (e.g. ordinary concrete, steel-scrap, ilmenite-limonite, and basalt-magnetite) to examine the shielding performance of the compound studied. The calculated MAC values for $Ti_{50}Cu_{30}Zr_{15}B_5$ were compared with those reported by researchers in Ref. [39] for the above-mentioned materials, and the results are given in Table 1. The HVL, TVL, and MFP display the ability of radiation to penetrate the shielding materials. The variation of HVL, TVL, and MFP parameters with the incident photon energies (0–15 MeV) were given in Fig. 12. It is desirable to have low HVL, TVL, and MFP values in the high-energy regions. While examining the HVL, TVL, and MFP values of the $Ti_{50}Cu_{30}Zr_{15}B_5$ alloy, it was seen that the Tenth Value Layer (TVL) is 0.009 cm at 1.5E-2 MeV energy photons, it is 12.5 cm with 15 MeV energy photons. Half-Value Layer (HVL) is 0.003 cm at 1.5E-2 MeV energy photons, while it is 3.76 cm with 15 MeV energy photons. It is seen that the HVL value for photons with 1 MeV energy is 2 cm. The 2 cm thick armor absorbs 99.82 % of the thermal neutrons. The Mean Free Path (MFP) is 0.004 cm for photons with 1.5E-2 MeV energy, it is 5.4 cm for photons with 15 MeV energy.

The values of the parameters obtained in this study for the given metal alloy were compared with some basic polymer shielding materials studied elsewhere in the literature [42] and were summarized in Table 2.

It is seen that the MFP value for 0.5 MeV photons is 2 cm. These results show that the $Ti_{50}Cu_{30}Zr_{15}B_5$ alloy is a successful shielding of 0.5 MeV energy photons and thermal neutrons. When the HVL, MFP and TVL values of the produced alloy are compared with the literature, the HVL and MFP value in all gamma energy values (75− x)Al–25Zn–xTi (x = 0, 0.01, 0.1 and 1 wt %) [43] alloy and HVL, TVL value (100-x)UPR-xTiO2 (x = 5,10,15, and 20 wt%) indicates a better gamma shielding than composite [44].

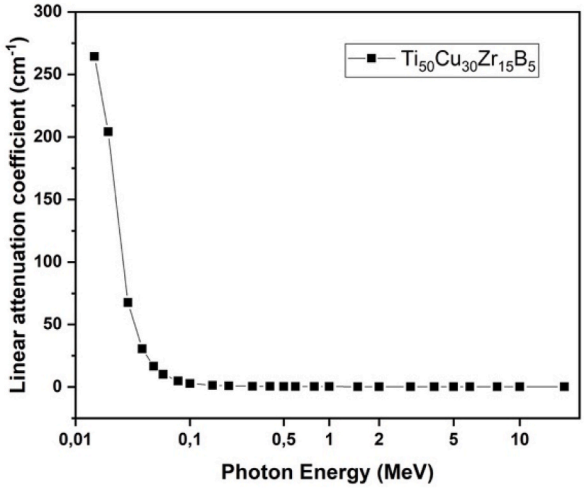

Fig. 9. Depicts the change of LAC with photon energy for $Ti_{50}Cu_{30}Zr_{15}B_5$ alloy.

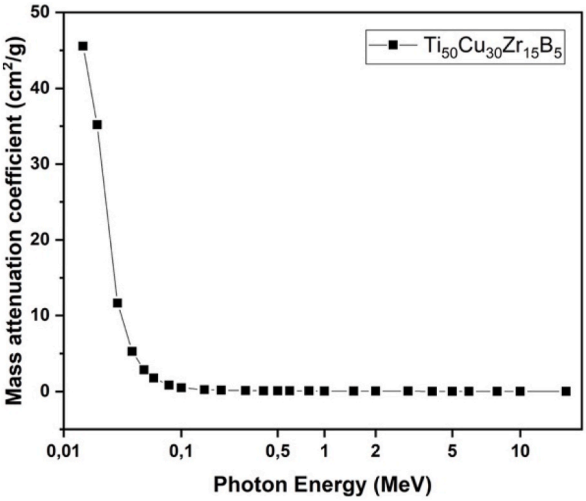

Fig. 10. Indicating the variation of mass attenuation coefficient with photon energy for $Ti_{50}Cu_{30}Zr_{15}B_5$ alloy.

4. Conclusions

In conclusion, the $Ti_{50}Cu_{30}Zr_{15}B_5$ alloy was successfully synthesized, and the physical properties such as crystal structure, morphology, microhardness, composition, and thermal behavior were investigated using different measurement techniques. The $Ti_{50}Cu_{30}Zr_{15}B_5$ alloy was discovered to be made of three distinct crystal phases by x-ray diffraction analysis: the hexagonal TiB phase, titanium-rich crystals of the tetragonal Ti_2Cu phase, and crystallites of the orthorhombic $Cu_{10}Zr_7$ phase. The conventionally solidified $Ti_{50}Cu_{30}Zr_{15}B_5$ alloy was characterized by grainy microstructure and the size of grains was found to be less than 10 μm. All the phases observed in the as-cast state were seen to be dissolved after solutionizing the alloy at 910 °C, which was confirmed by SEM micrographs. DTA analysis of the crystalline $Ti_{50}Cu_{30}Zr_{15}B_5$ alloy provided information about the melting temperature (910 °C) of the title alloy. The hardness value of $Ti_{50}Cu_{30}Zr_{15}B_5$ alloy calculated is 556 HV ($\pm$11). It was found that the phase transition temperature was reduced by incorporating Zr-into the Ti-alloy which was consistent with the earlier studies reported. The LAC value was 264.2 cm^{-1} at 1.5E-2 MeV energy photons and it decreased to 0.184 cm^{-1} at 15 MeV energy photons. The MAC value was 45.5 cm^2/g for 1.5E-2 MeV energy photons and was reduced to 0.032 cm^2/g at 15 MeV energy photons. Furthermore, the values of HVL, TVL, and MFP for the compound in this study were found to be impressive compared to other materials investigated. From the thermal neutron simulation results, it is seen that the 2 cm thick alloy can be a good neutron shield. Therefore, the $Ti_{50}Cu_{30}Zr_{15}B_5$ alloy was identified as a promising radiation shielding material.

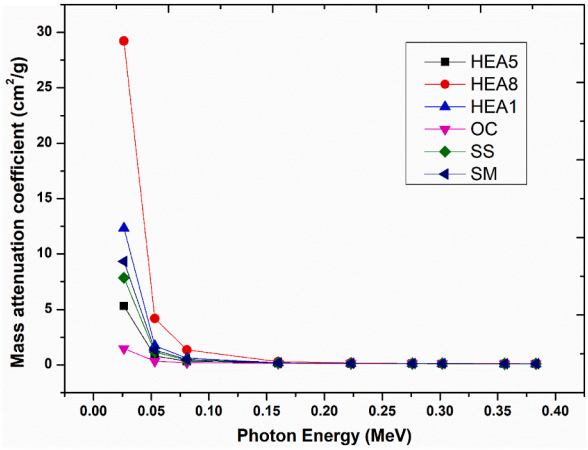

Fig. 11. Illustrating the variation of MAC of various compounds and alloys as a function of energy. The data has been reproduced from Refs. [40,41] for comparison.

Table 1
Comparison of calculated MAC values of $Ti_{50}Cu_{30}Zr_{15}B_5$ with those of the most widely used shielding materials like OC, SS, IL, and BM at different energies [39].

Energy (MeV)	$Ti_{50}Cu_{30}Zr_{15}B_5$, this study	Ordinary concrete	Stainless scrap	Ileminite-limonite	Basalt-magnetite
1.50×10^{-2}	10.24	7.079	37.92	29.64	20.47
5.00×10^{-2}	5.151	0.358	1.345	1.074	0.789
1.50×10^{-1}	0.124	0.142	0.176	0.165	0.157
5.00×10^{-1}	0.079	0.088	0.085	0.085	0.087
1.00×10^{0}	0.045	0.052	0.051	0.050	0.050
5.00×10^{0}	0.031	0.028	0.031	0.029	0.029
1.50×10^{1}	0.019	0.021	0.027	0.025	0.023

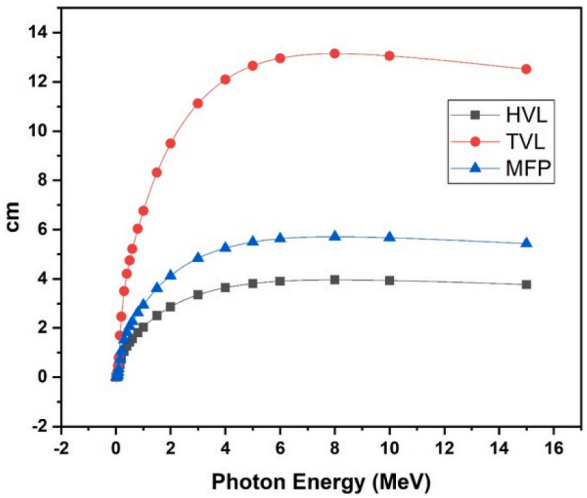

Fig. 12. Displaying the variation of MFP, HVL, and TVL with energy for $Ti_{50}Cu_{30}Zr_{15}B_5$ alloy.

Additional information

No additional information is available for this paper.

CRediT authorship contribution statement

Celal Kursun: Writing – review & editing, Writing – original draft, Supervision, Methodology, Conceptualization. **Meng Gao:**

Table 2
Comparison of the material's calculated HVL, TVL, and MFP values to those of several of the polymers studied by Kacal et al. [42].

Material	HVL (cm)		TVL (cm)		MFP (cm)	
Energy	0.1 MeV	1.5 MeV	0.1 MeV	1.5 MeV	0.1 MeV	1.5 MeV
$Ti_{50}Cu_{30}Zr_{15}B_5$	1.34	2.40	1.50	10.12	1.12	3.67
polyamide	2.02	6.12	7.05	19.0	3.02	7.10
Polyacrylonitrile	3.51	10.22	12.3	32.2	5.15	15.4
Polyvinylidenechloride	1.54	8.05	6.51	25.2	3.04	12.3
Polyaniline	2.53	8.51	12.2	28.3	3.20	13.1
polyethylene terephthalate	3.02	8.90	10.4	29.1	5.05	13.2
Polypyrole	2.64	7.55	8.34	25.2	4.30	12.1
Polytetrafluoroethylene	3.52	9.06	11.2	33.4	3.23	8.05

Writing – review & editing, Formal analysis. **Seda Guclu:** Writing – original draft, Investigation, Formal analysis. **Yasin Gaylan:** Writing – original draft, Software, Formal analysis. **Khursheed Ahmad Parrey:** Writing – review & editing, Writing – original draft, Investigation. **Ali Orkun Yalcin:** Writing – original draft, Formal analysis.

Declaration of competing interest

The authors declare the following financial interests/personal relationships which may be considered as potential competing interests:Celal Kursun reports financial support was provided by Kahramanmaras Sutcu Imam University. Meng Gao reports financial support was provided by Chinese Academy of Sciences Ningbo Institute of Materials Technology and Engineering. Celal Kursun reports a relationship with Kahramanmaras Sutcu Imam University that includes: board membership.

Acknowledgments

We extend our gratitude to the Kahramanmaras Sutcu Imam University for its generous financial support of our research program (Project No: 2022/7–15 M). Additionally, we would like to acknowledge the support received from the National Natural Science Foundation of China (No. 52201194) and 3315 Innovation Youth Talent program in Ningbo City (2021A-123-G).

References

[1] F. Akman, M.I. Sayyed, M.R. Kaçal, H.O. Tekin, Investigation of photon shielding performances of some selected alloys by experimental data, theoretical and MCNPX code in the energy range of 81 keV–1333 keV, J. Alloys Compd. 772 (2019) 516–524, https://doi.org/10.1016/J.JALLCOM.2018.09.177.
[2] M.I. Sayyed, F. Akman, I.H. Geçibesler, H.O. Tekin, Measurement of mass attenuation coefficients, effective atomic numbers, and electron densities for different parts of medicinal aromatic plants in low-energy region, Nucl. Sci. Tech. 29 (2018) 1–10, https://doi.org/10.1007/S41365-018-0475-0/TABLES/5.
[3] F. Akman, I.H. Geçibesler, M.I. Sayyed, S.A. Tijani, A.R. Tufekci, I. Demirtas, Determination of some useful radiation interaction parameters for waste foods, Nucl. Eng. Technol. 50 (2018) 944–949, https://doi.org/10.1016/J.NET.2018.05.007.
[4] M.I. Sayyed, Bismuth modified shielding properties of zinc boro-tellurite glasses, J. Alloys Compd. 688 (2016) 111–117, https://doi.org/10.1016/J.JALLCOM.2016.07.153.
[5] R. El-Mallawany, M.I. Sayyed, M.G. Dong, Comparative shielding properties of some tellurite glasses: Part 2, J. Non-Cryst. Solids 474 (2017) 16–23, https://doi.org/10.1016/J.JNONCRYSOL.2017.08.011.
[6] H.O. Tekin, T. Manici, Simulations of mass attenuation coefficients for shielding materials using the MCNP-X code, Nucl. Sci. Tech. 28 (2017) 1–4, https://doi.org/10.1007/S41365-017-0253-4/FIGURES/3.
[7] G. Lakshminarayana, S.O. Baki, K.M. Kaky, M.I. Sayyed, H.O. Tekin, A. Lira, I.V. Kityk, M.A. Mahdi, Investigation of structural, thermal properties and shielding parameters for multicomponent borate glasses for gamma and neutron radiation shielding applications, J. Non-Cryst. Solids 471 (2017) 222–237, https://doi.org/10.1016/J.JNONCRYSOL.2017.06.001.
[8] S.A.M. Issa, M.I. Sayyed, M.H.M. Zaid, K.A. Matori, Photon parameters for gamma-rays sensing properties of some oxide of lanthanides, Results Phys. 9 (2018) 206–210, https://doi.org/10.1016/J.RINP.2018.02.039.
[9] Y. Gaylan, B. Avar, M. Panigrahi, B. Aygün, A. Karabulut, Effect of the B4C content on microstructure, microhardness, corrosion, and neutron shielding properties of Al–B4C composites, Ceram. Int. 49 (2023) 5479–5488, https://doi.org/10.1016/J.CERAMINT.2022.10.071.
[10] Y. Gaylan, A. Bozkurt, B. Avar, Investigating thermal and fast neutron shielding properties of B4C, B2O3, Sm2O3, and Gd2O3 doped polymer matrix composites using Monte Carlo simulations, Süleyman Demirel Üniversitesi Fen Edebiyat Fakültesi Fen Dergisi. 16 (2021) 490–499, https://doi.org/10.29233/SDUFEFFD.933338.
[11] M. Donya, M. Radford, A. ElGuindy, D. Firmin, M.H. Yacoub, Radiation in medicine: origins, risks and aspirations, 2014, Glob Cardiol Sci Pract (2014) 437, https://doi.org/10.5339/GCSP.2014.57.
[12] S. Woosley, N. Abuali Galehdari, A. Kelkar, S. Aravamudhan, Fused deposition modeling 3D printing of boron nitride composites for neutron radiation shielding, J. Mater. Res. 33 (2018) 3657–3664, https://doi.org/10.1557/JMR.2018.316.
[13] Z. Soltani, A. Beigzadeh, F. Ziaie, E. Asadi, Effect of particle size and percentages of Boron carbide on the thermal neutron radiation shielding properties of HDPE/B4C composite: experimental and simulation studies, Radiat. Phys. Chem. 127 (2016) 182–187, https://doi.org/10.1016/J.RADPHYSCHEM.2016.06.027.
[14] A. Mesbahi, K. Verdipoor, F. Zolfagharpour, A. Alemi, Investigation of fast neutron shielding properties of new polyurethane-based composites loaded with B4C, BeO, WO3, ZnO, and Gd2O3 micro-and nanoparticles, Pol. J. Med. Phys. Eng. 25 (2019) 211–219, https://doi.org/10.2478/PJMPE-2019-0028.
[15] O. Olarinoye, C. Oche, Gamma-ray and fast neutron shielding parameters of two new titanium-based bulk metallic glasses, Iran. J. Med. Phys. 18 (2021) 139–147, https://doi.org/10.22038/IJMP.2020.42684.1635.
[16] Lead poisoning, (n.d.). https://www.who.int/news-room/fact-sheets/detail/lead-poisoning-and-health (accessed April 24, 2023).
[17] J.H. Oh, S.H. Gwon, T.H. Kim, J.Y. Sun, S. Choi, Synthesis of titanium boride nanoparticles and fabrication of flexible material for radiation shielding, Curr. Appl. Phys. 31 (2021) 151–157, https://doi.org/10.1016/J.CAP.2021.08.009.
[18] I. Bilobrov, V. Trachevsky, Approach to modify the properties of titanium alloys for use in nuclear industry, J. Nucl. Mater. 415 (2011) 222–225, https://doi.org/10.1016/J.JNUCMAT.2011.05.056.

[19] O. Çuvalcı, T. Varol, S.B. Akçay, O. Güler, A. Çanakçı, Effect of ball mill time and wet pre-milling on the fabrication of Ti powders by recycling Ti machining chips by planetary milling, Powder Technol. 426 (2023), 118637, https://doi.org/10.1016/j.powtec.2023.118637.
[20] O. Senkov, S. Senkova, D. Miracle, C. Woodward, Mechanical properties of low-density, refractory multi-principal element alloys of the Cr–Nb–Ti–V–Zr system, Mater. Sci. Eng., A 565 (2013) 51–62.
[21] O.A. Waseem, H.J. Ryu, Combinatorial development of the low-density high-entropy alloy $Al_{10}Cr_{20}Mo_{20}Nb_{20}Ti_{20}Zr_{10}$ having gigapascal strength at 1000 c, J. Alloys Compd. 845 (2020), 155700.
[22] P. Chauhan, S. Yebaji, V.N. Nadakuduru, T. Shanmugasundaram, Development of a novel lightweight $Al_{35}Cr_{14}Mg_6Ti_{35}V_{10}$ high entropy alloy using mechanical alloying and spark plasma sintering, J. Alloys Compd. 820 (2020), 153367.
[23] V.K. Pandey, Y. Shadangi, V. Shivam, J. Basu, K. Chattopadhyay, B. Majumdar, B. Sarma, N.K. Mukhopadhyay, Synthesis, characterization and thermal stability of nanocrystalline MgAlMnFeCu low-density high-entropy alloy, Trans. Indian Inst. Met. 74 (1) (2021) 33–44.
[24] M.C. Team, MCNP-A General Monte Carlo N-Particle Transport Code, Version 5 Volume I: Overview and Theory X-5 Monte Carlo Team, 2003.
[25] M.I. Sayyed, K.A. Mahmoud, S. Islam, O.L. Tashlykov, E. Lacomme, K.M. Kaky, Application of the MCNP 5 code to simulate the shielding features of concrete samples with different aggregates, Radiat. Phys. Chem. 174 (2020), 108925, https://doi.org/10.1016/J.RADPHYSCHEM.2020.108925.
[26] R. El-Mallawany, M.I. Sayyed, M.G. Dong, Y.S. Rammah, Simulation of radiation shielding properties of glasses contain PbO, Radiat. Phys. Chem. 151 (2018) 239–252, https://doi.org/10.1016/J.RADPHYSCHEM.2018.06.035.
[27] L. Xie, C. Jiang, V. Ji, Thermal relaxation of residual stresses in shot peened surface layer of (TiB + TiC)/Ti–6Al–4V composite at elevated temperatures, Mater. Sci. Eng., A 528 (2011) 6478–6483, https://doi.org/10.1016/J.MSEA.2011.04.075.
[28] A.F. Albisetti, C.A. Biffi, A. Tuissi, Synthesis and structural analysis of copper-zirconium oxide, 195. 6, Metals 2016 6 (2016) 195, https://doi.org/10.3390/MET6090195.
[29] V.M. Villapun, F. Esat, S. Bull, L.G. Dover, S. Gonzalez, Tuning the mechanical and antimicrobial performance of a Cu-based metallic glass composite through cooling rate control and annealing, Vol. 10, Page 506, Materials 2017 10 (2017) 506, https://doi.org/10.3390/MA10050506.
[30] S. Zherebtsov, M. Ozerov, M. Klimova, N. Stepanov, T. Vershinina, Y. Ivanisenko, G. Salishchev, Effect of high-pressure torsion on structure and properties of Ti-15Mo/TiB metal-matrix composite, 11, Page 2426, Materials 2018 11 (2018) 2426, https://doi.org/10.3390/MA11122426.
[31] X. Wang, L. Wang, L.S. Luo, Y.J. Xu, X.Z. Li, R.R. Chen, Y.Q. Su, J.J. Guo, H.Z. Fu, Hydrogen induced softening and hardening for hot workability of (TiB + TiC)/Ti-6Al-4V composites, Int. J. Hydrogen Energy 42 (2017) 3380–3388, https://doi.org/10.1016/J.IJHYDENE.2017.01.030.
[32] K. Tomolya, Ti-Cu-Based amorphous powders produced by ball-milling, Mater. Sci. Forum 879 (2017) 1974–1979, https://doi.org/10.4028/WWW.SCIENTIFIC.NET/MSF.879.1974.
[33] C. Kursun, M. Gögebakan, Y. Gencer, Microstructural characterization of rapidly solidified $Cu_{50}Zr_{40}Ni_5Ti_5$ amorphous alloy, J. Alloys Compd. 643 (2015) S33–S38, https://doi.org/10.1016/j.jallcom.2014.10.041.
[34] D. Dickel, C.D. Barrett, R.L. Carino, M.I. Baskes, M.F. Horstemeyer, Mechanical instabilities in the modeling of phase transitions of titanium, Model. Simulat. Mater. Sci. Eng. 26 (2018), 065002, https://doi.org/10.1088/1361-651X/AAC95D.
[35] S. Liang, Y. Zhou, L. Yin, Strengthening/weakening action of Zr on stabilizers of Ti alloys and its effect on phase transition, J. Mater. Eng. Perform. 30 (2021) 876–884, https://doi.org/10.1007/S11665-020-05408-2/FIGURES/9.
[36] M.J. Bermingham, S.D. McDonald, K. Nogita, D.H. St John, M.S. Dargusch, Effects of boron on microstructure in cast titanium alloys, Scripta Mater. 59 (2008) 538–541, https://doi.org/10.1016/J.SCRIPTAMAT.2008.05.002.
[37] A.I. Gorunov, Laser pulse alloying the surface of Ti-5.5Al-2Zr-1Mo-1V by boron carbide particles, Int. J. Adv. Manuf. Technol. 105 (2019) 719–731, https://doi.org/10.1007/S00170-019-04200-4/FIGURES/19.
[38] J. Abenojar, M.A. Martinez, F. Velasco, Effect of the boron content in the aluminium/boron composite, J. Alloys Compd. 422 (2006) 67–72, https://doi.org/10.1016/J.JALLCOM.2005.11.042.
[39] I.I. Bashter, Calculation of radiation attenuation coefficients for shielding concretes, Ann. Nucl. Energy 24 (1997) 1389–1401, https://doi.org/10.1016/S0306-4549(97)00003-0.
[40] B. Subedi, J. Paudel, T.R. Lamichhane, Gamma-ray, fast neutron, and ion shielding characteristics of low-density and high-entropy Mg–Al–Ti–V–Cr–Fe–Zr–Nb alloy systems using Phy-X/PSD and SRIM programs, Heliyon 9 (7) (2023).
[41] O. Senkov, S. Senkova, D. Miracle, C. Woodward, Mechanical properties of low-density, refractory multi-principal element alloys of the Cr–Nb–Ti–V–Zr system, Mater. Sci. Eng., A 565 (2013) 51–62.
[42] M.R. Kaçal, F. Akman, M.I. Sayyed, Evaluation of gamma-ray and neutron attenuation properties of some polymers, Nucl. Eng. Technol. 51 (3) (2019) 818–824.
[43] M. Sirin, The effect of titanium (Ti) additive on radiation shielding efficiency of $Al_{25}Zn$ alloy, Prog. Nucl. Energy 128 (2020), 103470, https://doi.org/10.1016/J.PNUCENE.2020.103470.
[44] C.V. More, S.N. Botewad, F. Akman, O. Agar, P.P. Pawar, UPR/Titanium dioxide nanocomposite: preparation, characterization and application in photon/neutron shielding, Appl. Radiat. Isot. 194 (2023), 110688, https://doi.org/10.1016/J.APRADISO.2023.110688.